

VIP Very Important Paper

www.batteries-supercaps.org

Li_{6.25}Al_{0.25}La₃Zr_{1.75}Nb_{0.25}O₁₂ Nanofiber Fillers Reinforced PVDF-HFP-Based Bilayer Composite Solid-State Electrolytes

Minghua Chen,*^[a] Wannian Liu,^[a] Yixin Wu,^[a] Yulong Liu,^[a] Yang Wang,^[a] and Zhen Chen*^[a]

Composite solid-state electrolytes (CSEs) combining the advantages of polymer and ceramic electrolytes, are regarded as highly promising candidates for solid-state lithium metal batteries (SSLMBs). However, selecting appropriate polymer and ceramic materials, along with an effective combination method, is crucial in determining the performance of CSEs. To address the challenges of lithium dendrite inhibition and compatibility with cathodes simultaneously, herein, we have constructed a bilayer CSE based on poly(vinylidene fluoride)-hexafluoropropylene (PVDF-HFP). Al/Nb co-doped Li_{6.25}Al_{0.25}La₃Zr_{1.75}Nb_{0.25}O₁₂ (LALZNO) nanofibers prepared by an electrostatic spinning technique, are incorporated as fillers to create high-throughput

Li⁺ transport pathways and enhance the overall performance of the CSE. Furthermore, polypropylene carbonate is introduced on the anode side of the CSE to enhance the wettability of lithium metal/CSE interface, thus improving the stability of lithium upon cycling. On the cathode side, succinonitrile is added to inhibit the crystallization of PVDF-HFP and facilitate the fast Li⁺ transport. Consequently, the Li||Li cells demonstrate stable plating-stripping performance at 0.1 mA cm⁻² for >520 h. In addition, the Li||LiFePO₄ full cells show improved cycling and rate performance. This work validates the effectiveness of developing bilayer CSEs and showcases their potential application in SSLMBs.

Introduction

The increasing of global population and the rapid development of industrialized economies have accelerated the consumption of energy, further exacerbated by the shift from traditional fossile fuels to renewable clean energy sources.^[1] Among various energy storage technologies, lithium-ion batteries (LIBs) have emerged as a new and efficient solution for diverse applications, including portable electronic devices, electric vehicles, smart grids, and other fields.^[2] However, despite their widespread use, LIBs face limitations in terms of energy density, which is gradually reaching its maximum potential. Additionally, traditional organic liquid electrolytes and polyolefin separators lack thermal stability, making the batteries susceptible to safety issues such as liquid leakage, high-temperature combustion, and even explosions. These safety concerns can lead to short circuits and accidents.^[3]

To address the aforementioned challenges, extensive attention has been directed towards solid-state lithium metal batteries (SSLMBs), which offer higher energy density, longer cycle life, and improved safety compared to traditional LIBs.^[4] Lithium metal, as an anode material in lithium metal batteries (LMBs), has garnered significant interest due to its exceptional properties, including ultra-high specific capacity (3860 mAh g⁻¹), low density (0.53 g cm⁻³), and the lowest potential (-3.04 V vs H⁺/H₂). The utilization of lithium metal holds great promise for

enhancing the energy density of batteries compared to the currently commercialized graphite anode in LIBs.^[5] The development of SSLMBs necessitates the integration of solid-state electrolytes (SSEs), which play a crucial role in providing excellent stability, suppressing lithium dendrite formation, and ensuring compatibility with high-voltage cathodes. SSEs are indispensable components of the SSLMB system due to notable advantages in reducing the amount of organic solvent, while maintaining electrochemical, thermal, and mechanical stability, even under conditions of cracking, extrusion, or perforation, thereby providing a potential solution to address safety concerns.^[6,7-11]

Polymer-based solid-state electrolytes (PSEs) are vital components of SSEs, offering several advantageous characteristics, including cost-effectiveness, high plasticity, mechanical flexibility, compatibility with electrode materials, and suitability for mass manufacturing. Among them, poly(vinylidene fluoride)-hexafluoropropylene (PVDF-HFP) stands out due to its high dielectric constant and relatively low degree of crystallinity, which facilitate the dissociation of lithium salts.^[12-14] Additionally, the electron-absorbing functional groups (-C-F) enable stable interactions with lithium metal anode, resulting in superior electrochemical and thermal stability. Polypropylene carbonate (PPC), a polycarbonate copolymer of propylene oxide and carbon dioxide, has garnered significant attention as a green material. The conversion of PPC to propylene carbonate and hydroxyl-containing short chains by lithium metal greatly enhances the wettability between PPC and lithium, ensuring a compatible interface. However, PSEs often exhibit relatively high degrees of crystallinity, which hinder efficient Li⁺ transport. Moreover, the limited mechanical strength of PSEs fails to effectively suppress the growth of lithium dendrites, posing challenges for the operation of SSLMBs across a wide temperature range.^[15-17]

[a] M. Chen, W. Liu, Y. Wu, Y. Liu, Y. Wang, Z. Chen

Key Laboratory of Engineering Dielectric and Applications (Ministry of Education), School of Electrical and Electronic Engineering, Harbin University of Science and Technology, Harbin, Heilongjiang 150080, China
E-mail: mhchen@hrbust.edu.cn

chen.zhen@hrbust.edu.cn

Supporting information for this article is available on the WWW under
<https://doi.org/10.1002/batt.202400379>

Composite solid-state electrolytes (CSEs) that incorporate inorganic fillers into a polymer matrix have emerged as highly promising electrolyte candidates for SSLMBs, leveraging the advantages of both components.^[18] Among a series of ceramic fillers, Li₇La₃Zr₂O₁₂ (LLZO) stands out due to its wide electrochemical stability window and superior compatibility with lithium metal anodes. The cubic phase of LLZO (c-LLZO) exhibits superior ionic conductivity compared to the tetragonal phase (t-LLZO). To promote the formation and stabilization of the cubic phase, elements such as Al, Nb, Ce, etc., are commonly doped into LLZO.^[19–22] However, to fully utilize the high energy density of SSLMBs, it is necessary to combine a low-potential lithium anode with a high-voltage positive cathode. Currently, achieving compatibility with both high-voltage cathodes and lithium metal anodes still remains a great challenge for a single solid electrolyte system.

To address these challenges, the strategy of designing multilayer electrolyte structures has attracted significant attention. SSEs with different functions can form a composite layered structure that ensures good compatibility, effectively resolving the interface issues between the cathode and anode. CSEs with multilayer structures have gained attention for their ability to enhance the interfacial contact between the SSE and the electrode, meet the requirements of high ionic conductivity and good mechanical flexibility/strength, and improve the overall performance of SSLMBs.

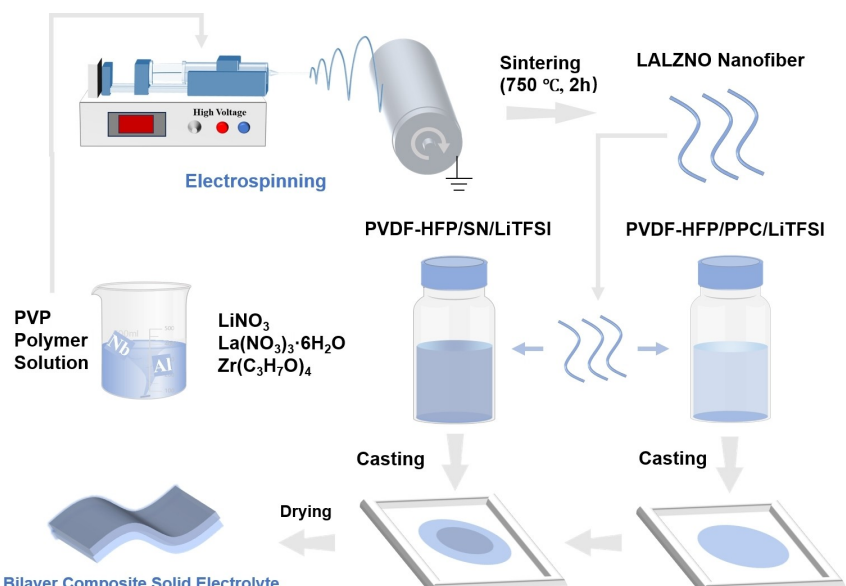
Herein, Li_{6.25}Al_{0.25}La₃Zr_{1.75}Nb_{0.25}O₁₂ (LALZNO) nanofibers prepared by electrospinning were incorporated as fillers to obtain the PVDF-HFP-based CSE. The nanofiber structures as well as the Al/Nb co-doping of LALZNO effectively improve the ionic conductivity, lithium-ion transference number, thermal stability, and electrochemical stability window. The construction of bilayer CSE, achieved by blending succinonitrile (SN) and PPC into the cathode and the anode sides of the CSEs (Scheme 1), respectively, contributes to further improved ionic conductivity

and high compatibility against lithium over cycling. Introducing SN into the cathode side alleviates side reactions with the lithium anode, increase conductivity, and enhances the antioxidant capacity of the CSE. PPC is introduced into the anode side of the CSE to better wet the lithium metal/CSE interface and reduce the interfacial contact resistance. The effectiveness of this design is validated by the significantly enhanced electrochemical performance observed in both Li||Li symmetric cells and Li||LiFePO₄ (LFP) full cells. These findings reflect the efficacy of ceramic fiber fillers in improving the performance of PSE and verify the potential of bilayer CSEs for the application of SSLMBs.

Results and Discussion

Figure 1a presents the scanning electron microscope (SEM) image of precursor fibers, highlighting their distinct and uniform morphology. To investigate the formation process of LALZNO nanofibers, a thermogravimetric (TG) analysis was conducted (Figure 1b). The precursor fibers exhibit a weight loss of nearly 9.6 wt% when the temperature increases to 200 °C, presumably due to the volatilization of the N,N-dimethylformamide (DMF) solvent. A sharp increase in weight loss occurs at 300 °C, which is attributed to the decomposition of poly(vinylpyrrolidone) (PVP). Further weight loss between 300–500 °C may be due to the decomposition of nitrates. Beyond 750 °C, a minor weight loss is observed, mainly attributed to the loss of lithium at high temperatures.^[23,24]

Based on the TG results, sintering procedures were set at varying temperatures (i.e., 650 °C, 750 °C, 850 °C). Figures 1c and S1(a–e) depict the ceramic fibers, highlighting the significant influence of the sintering temperature on the surface morphology and crystal structure of the interconnected LALZNO nanofibers. At a sintering temperature of 650 °C (Figure S1a), the



Scheme 1. Schematic illustration of the preparation of a bilayer CSE.

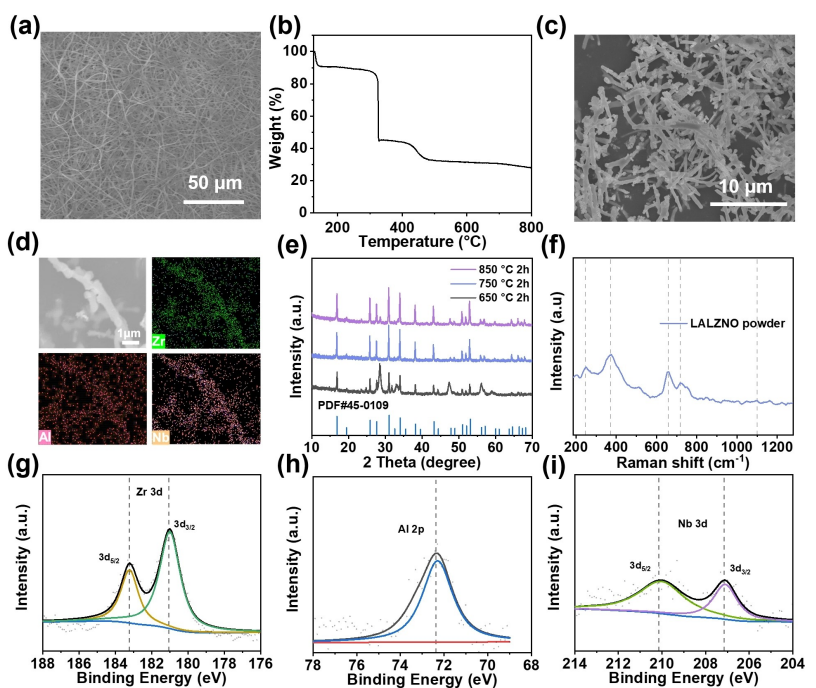


Figure 1. SEM images of (a) the precursor of LALZNO fiber mat, and (c) the LALZNO nanofibers sintered at 750 °C. (d) SEM image and its corresponding EDS mapping of Zr, Al, and Nb elements of LALZNO fibers. (b) The TG profile of precursor LALZNO fiber mat. (e) XRD patterns of LALZNO fibers sintered at different temperatures. (f) Raman spectrum, and (g-i) XPS spectra of Zr 3d, Al 2p, and Nb 3d of LALZNO fibers.

formed inorganic ceramics exhibit a coral-like shape, with small particles that are not yet fully interconnected, as seen in the magnified image (Figure S1b). This suggests that the sintering temperature was not sufficiently high to facilitate proper bonding of grain boundaries on the ceramic surface. In contrast, at 750 °C (Figure S1c), the overall ceramic surface morphology demonstrates a uniformly interconnected fiber structure. Additionally, Figure 1c shows a clearly intact fiber shape. This indicates that the sintering temperature of 750 °C allows for the preservation of fiber structure without compromising its integrity or causing structural failure. At 850 °C, the ceramics lose their distinct fiber structure and present a blocky appearance (Figure S1d and e). Thus, to maintain the intact fiber structure and prevent structural failure and nanofiber agglomeration, the sintering temperature of 750 °C was selected as the optimal condition.^[25–27]

Figure 1c presents the SEM and energy-dispersive X-ray spectrometer (EDS) mapping of representative LALZNO fibers sintered at 750 °C. The fiber structure exhibits a diameter of approximately 600 nm. The EDS mapping pattern of LALZNO fibers confirms the uniform distribution of La, Zr, Al, and Nb in the ceramic powder, indicating the successful doping of Al and Nb. Figure 1e shows the X-ray diffractometer (XRD) patterns of samples sintered at different temperatures. The cubic phase LALZNO is not fully formed after sintering at 650 °C. An additional peak appears at 28.63° after sintering at 850 °C, which is assigned to the impurity phase of La₂Zr₂O₇. The XRD pattern of LALZNO sintered at 750 °C is well consistent with the LLZO cubic phase (PDF#45-0109).^[28,29] Figure S1g illustrates the XRD pattern of LLZO (prepared by the same preparation

procedure as that of the LALZNO). The diffraction peaks of LLZO reveal the presence of both cubic and tetragonal phases. It is well known that the tetragonal phase features with much poor ionic conductivity. This reflects that the Al/Nb doping favors the formation of cubic phase crystals. Raman spectrum further identifies its cubic phase structure (Figure 1f). The peaks at 248.1 and 371.7 cm⁻¹ correspond to the LiO₆ and LiO₄ octahedral units, respectively, and the signals at 659.6 and 717.2 cm⁻¹ correspond to the stretching of O–Zr–O bonds and Nb–O bonds, respectively. In addition, the weak peak at ~1100 cm⁻¹ belongs to Li₂CO₃.^[30]

X-ray photoelectron spectroscopy (XPS) was performed to examine the surface chemistry of LALZNO (Figures 1g–i and S2a–d). The Zr 3d spectrum (Figure 1g) clearly displays two peaks corresponding to the double-state spin orbitals of Zr–O bonds, i.e., 3d_{5/2} (181.1 eV) and 3d_{3/2} (183.2 eV). The La 3 d XPS spectrum (Figure S2a) shows a double-state spin-orbit splitting (3d_{5/2} and 3d_{3/2} at 835.1/839.4 and 851.9/856.1 eV, respectively). The signals of Al and Nb indicate their successfully doping into the ceramics (Figure 1h and i). Figure S2b presents the C 1 s XPS spectrum, with signals at 285.2 and 290.3 eV corresponding to C–C (amorphous carbon) and Li₂CO₃, respectively. The O 1s XPS spectrum (Figure S2c) demonstrates two peaks at 531.4 and 532.2 eV corresponding to the metal oxides and Li₂CO₃ impurity, respectively. Evident from the Li 1s spectrum (Figure S2d), the peaks centered at 53.8 and 54.3 eV are attributed to the Li–O and Li₂CO₃ impurity phases.^[31,32]

The bilayer CSE membranes (denoted as PPL) and the bilayer pure polymer membrane without LALZNO nanofiber (denoted as PP) were prepared by a solution casting method.

Digital photographs of the PPL and PP membranes (Figure 2a) show uniform surfaces and superior flexibility. Figure 2b and c depict the surface and cross-sectional SEM images, respectively, of the PPL membrane. The PPL membrane exhibits a notably smooth surface, with LALZNO fibers uniformly distributed and interconnected within the polymer matrix, contributing to the formation of fast Li⁺ conduction channels and enhanced ionic conductivity.^[33] In sharp contrast, the surface of the PP membrane (Figure S3a) exhibits large voids and clumped polymer agglomerates, resulting in a structure with significant defects. The cross-sectional image (Figure S3b) reveals numerous larger bubbles within the polymer, hindering the transport of lithium ions.^[34] The EDS mapping of the La, Zr, Nb, and Al elements further confirms the presence of well-dispersed ceramic fibers within the polymer matrix (Figure 1d).

To determine the optimal doping amount of LALZNO, the ionic conductivities of the monolayer CSE membranes (denoted as PL-X, where X represents the percentage of filler amount) were examined in symmetric blocking SS|CSE|SS cells (SS: stainless steel) at room temperature. Evident from Figure 3a, the ionic conductivity of monolayer CSEs initially increases and then decreases with increasing doping amounts. The PL-0 membrane exhibits the lowest ionic conductivity, ca., $3.82 \times 10^{-5} \text{ Scm}^{-1}$, while the PL-15 membrane achieves the highest value ($1.49 \times 10^{-4} \text{ Scm}^{-1}$). The observed change in conductivity can be attributed to the dissociation of LiTFSI promoted by the inorganic ceramic fiber filler. Additionally, the fiber structure creates linear and efficient Li⁺ conduction channels, thus increasing the ionic conductivity. However, further increasing the filler content would lead to filler agglomeration within the CSE, which is unfavorable for Li⁺ transport and leads to decreased ionic conductivity.^[35,36] Based on the screening of ionic conductivity, 15 wt% of LALZNO filler was selected to be the optimized parameter, which also serves as a guiding parameter for the preparation of bilayer CSEs.

According to the Nyquist plots of bilayer CSEs demonstrated in Figure 3b, the room temperature ionic conductivities of PP and PPL membranes were calculated to be $2.9 \times 10^{-4} \text{ Scm}^{-1}$ and $5.7 \times 10^{-4} \text{ Scm}^{-1}$, respectively. The overall ionic conductivities of the bilayer CSE membranes are clearly higher than those of the monolayers. Such an improvement could be due to the following reasons: 1) Blending of PPC and SN with PVDF-HFP further reduces the crystallization of the PVDF-based polymers and improves the polymers' segmental motion, which is favorable for Li⁺ transport. 2) The interfacial reaction between PPC and Li metal leads to *in situ* gelation of PPC, which enhances the interfacial compatibility and decreases the interfacial resistance.^[37] The temperature-dependent ionic conductivity results of mono- and bilayer CSE membranes (Figure 3c) reveal the characteristic Arrhenius behavior of all electrolyte membranes. The activation energies of PP and PPL membranes were calculated to be 0.307 and 0.259 eV, respectively. On the other hand, the values are 0.301 and 0.406 eV for monolayer PL-0 and PL-15 membranes. The lowest activation energy of PPL suggests its superior capability of reducing the ion transport barrier and promoting Li⁺ transport kinetics.^[38]

Subsequently, the oxidation stability of both mono- and bilayer CSE membranes was determined by linear scanning voltammetry (LSV) curves (Figure 3d). The oxidation potentials were determined to be 4.10 V (PL-0), 4.72 V (PL-15), 4.64 V (PP), and 4.78 V (PPL), respectively. It is seen that incorporating LALZNO filler consistently allows for higher voltage tolerance in both mono- and bilayer CSEs. The PPL membrane achieves the highest oxidation stability, thanks to the introduction of SN component that further increases the oxidative stability.^[39]

The Li⁺ transference number (t_{Li^+}) was determined based on the Evans-Vincent-Bruce method in a Li|SCE|Li symmetric cell. The PPL (Figure 3e) achieves a t_{Li^+} value of 0.47, higher than that of the PP (0.32; Figure S4a), PL-0 (0.26; Figure S4b) and PL-15 (0.43; Figure S4c). The relatively higher t_{Li^+} values of CSEs with respect to the pure polymer may be related to the

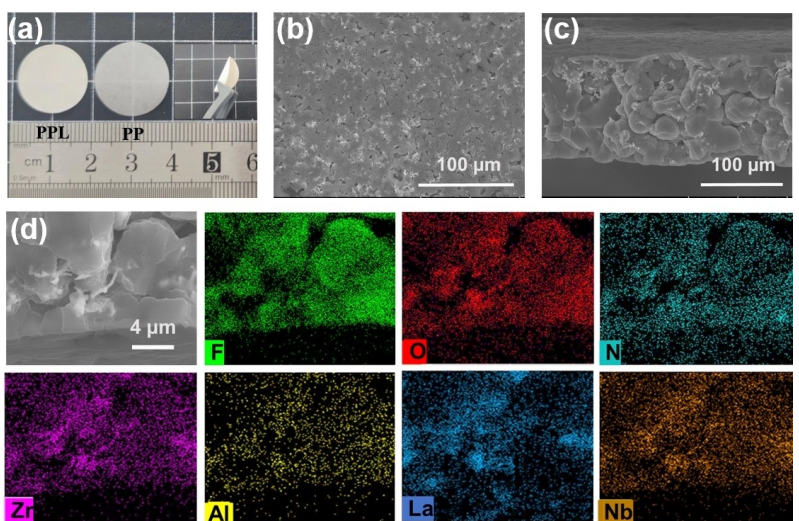


Figure 2. (a) Digital photographs of PPL and PP membranes. SEM images of (b) surface and (c) cross-sectional view of PPL. (d) SEM image and EDS mapping results of F, O, N, Zr, Al, La, and Nb of PPL.

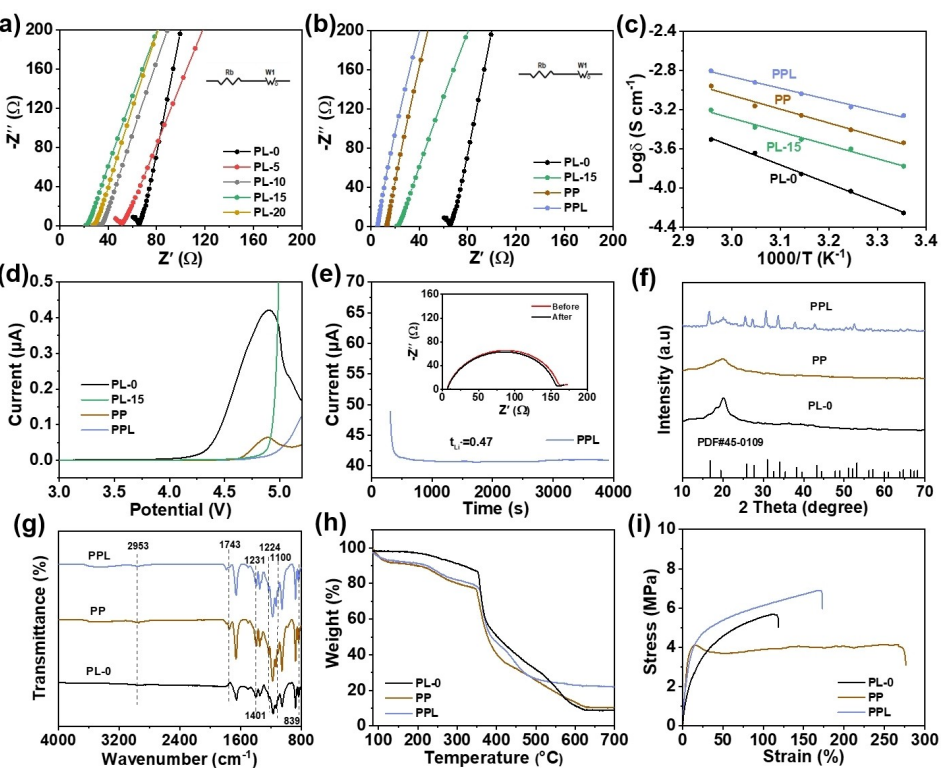


Figure 3. Nyquist plots of (a) various monolayer CSEs with different ceramic filler doping amounts and (b) bilayer CSEs. (c) Arrhenius plots and (d) LSV curves of monolayer and bilayer CSE membranes. (e) The determination of t_{Li^+} of PPL membrane. (f) The XRD patterns, (g) FT-IR spectra, (h) TG profiles, and (i) mechanical stability comparison of PPL, PP, and PL-0 membranes.

TFSI⁻ trapping effect induced by the acidic surface sites of LALZNO fillers, as well as the additional Li⁺ conduction paths provided by LALZNO fibers. Additionally, SN can facilitate the dissociation of LiTFSI and the C=O groups in PPC form complexes with TFSI⁻, both of which increase the concentration of free Li-ions and yield higher t_{Li^+} of bilayer electrolyte membrane compared to that of the monolayer.

Figure 3f illustrates the XRD patterns of PPL, PP, and PL-0 membranes. The peaks observed at 18.6° and 20.3° correspond to the characteristic diffraction peaks of PVDF-HFP. A decrease in the intensity of the crystalline peak at 18.6° in PP compared to PL-0 indicates interchain interactions between the polymers, leading to a more amorphous polymer phase after blending PVDF-HFP with PPC and SN. Furthermore, the incorporation of LALZNO nanofiber fillers results in a weaker peak intensity and broader peak width at 20.3°. This suggests a reduction in the polymer's crystallinity and an increase in its amorphous nature, which typically promotes ion transport. The XRD patterns of the prepared CSE membranes do not show any new peaks, indicating a stable physical interaction of LALZNO filler with the polymer matrix.^[40]

As illustrated in Figure 3g, the characteristic peaks of C–F stretching and –CH₂ stretching of PVDF-HFP are detected at 1401 cm⁻¹ and 839 cm⁻¹, respectively. The stretching vibrations of C=O (1743 cm⁻¹), C–O (1224 cm⁻¹), C–O–C (1231 cm⁻¹), and C–H (2953 cm⁻¹) are assigned to the characteristic absorption bands of PPC. The Fourier transform infrared spectroscopy (FT-IR) spectra confirm the mixing of PPC with PVDF-HFP. Some

bands are broadened after the addition of fillers, suggesting that the LALZNO fillers can affect the crystallization properties of the polymer chains.^[41]

TG analyses were performed to evaluate the thermal stability of PPL, PP, and PL-0 membranes as demonstrated in Figure 3h. When the temperature increases to 150°C, the weight loss of PPL and PP membranes is about 7.4 wt% and 8.6 wt%, respectively, a result of decomposition of the thermally unstable SN, volatilization of DMF and the removal of absorbed water. When the temperature reaches 250°C, a gradual weight loss is evidenced for both PPL and PP membranes, due to the decomposition of the PPC. Further heating to 350°C, the weights of all samples drop dramatically, owing to the decomposition of PVDF-HFP with LiTFSI. In addition, the weight loss beyond 450°C may be related to further decomposition of LiTFSI and lower degrees of polymer crystallinity. The residual weights were calculated to be 22.3, 12.1, and 8.85 wt%, respectively.

The evaluation of mechanical properties of PPL, PP, and PL-0 membranes is shown in Figure 3i. The PL-0 membrane exhibits a maximum stress of 5.6 MPa and a strain of 114%. The stress of the PP membrane decreases to 4.1 MPa due to the lower mechanical strength of PPC and SN, as well as the reduced crystallinity of the PVDF-HFP matrix. However, the introduction of PPC leads to a higher elongation of 280%. By incorporating LALZNO fillers into the PPL membrane, the maximum stress significantly increases to 6.9 MPa, accompanied by a strain of 175%. These values are higher than those of the

PL-0 membrane. Thanks to the reinforcement of LALZNO fillers, more reliable mechanical properties are achieved, facilitating the inhibition of Li dendrites growth, thereby enhancing the safety and reliability of SSLMBs.^[42]

Figure 4a presents the critical current density (CCD) test results. When revealed in a time-constant mode, the CCD of Li|PPL|Li cell reaches 0.4 mA cm^{-2} , which is higher than that of the Li|PP|Li (0.2 mA cm^{-2}) and Li|PL-0|Li (0.1 mA cm^{-2}) cells, highlighting the superior lithium-ion transport kinetics and stronger capability in preventing lithium dendrites of PPL compared to its counterparts. In addition, a capacity-constant mode was adopted to evaluate the CCD values by steadily increasing the current density from 0.1 to 0.6 mA cm^{-2} with a fixed capacity of 0.3 mAh cm^{-2} . The Li|PPL|Li cell achieves a high CCD over 0.6 mA cm^{-2} (Figure 4b). In stark contrast, the Li|PP|Li cell short circuits at merely 0.1 mA cm^{-2} with a deposition capacity of approximately 0.2 mAh cm^{-2} .

The interfacial stability of various CSEs against lithium metal was assessed by lithium stripping and plating test at 0.1 mA cm^{-2} . Five cycles at a current density of 0.05 mA cm^{-2} were initially used to activate the electrolyte and facilitate the formation of a stable lithium/electrolyte interface/interphase. The Li|PPL|Li symmetric cell exhibits stable and uninterrupted cycling for over 520 h. In contrast, the Li|PP|Li symmetric cell experiences a rapid increase in overpotential after 150 h (Figure 4c). The Li|PL-0|Li symmetric cell, compared to the bilayer CSE-based cells, gradually gets short-circuited after only 50 h of cycling, indicating its inferior ability to prevent the formation

and penetration of lithium dendrites. The longer and stable cycling observed in the bilayer PP membrane compared to the monolayer PL-0 membrane is primarily attributed to the positive interaction between PPC and the lithium anode. The in situ gelation of PPC reduces interfacial impedance, and the reaction degradation products enable PPC to expand, better accommodating the volume change of the lithium metal anode during cycling. This results in the formation of a stable solid electrolyte interphase (SEI) and promotes the homogeneous deposition of Li^+ on the anode.^[43] The further extended cycling lifetime observed in the Li|PPL|Li cell can be attributed to the lithium dendrite inhibition and the anion binding properties of LALZNO fillers, which provide additional channels to maintain the uniformity of Li^+ distribution and adsorb anions on the surface. From the inset, it is seen that the average polarization voltage of Li|PPL|Li cell is much smaller ($\sim 40 \text{ mV}$) with respect to that of the Li|PP|Li cell ($\sim 100 \text{ mV}$). At a current density of 0.2 mA cm^{-2} , the Li|PPL|Li cell exhibits a stable and flat plateau for more than 250 h of cycling (Figure 4d). In contrast, the overpotential of Li|PP|Li cell starts to increase rapidly after 80 h, reaching to 0.8 V after 130 h of cycling. The extended view curve of the Li|PP|Li cell from 100 h to 180 h is displayed in Figure 4e, from which it is seen that the overpotential remains constant at $\sim 0.1 \text{ V}$.

To investigate the morphology of electrolyte membranes and lithium metal after cycling, fresh Li|PP|Li and Li|PPL|Li symmetric cells were assembled for 50 cycles at 0.2 mA cm^{-2} and 0.2 mAh cm^{-2} . These cells were subsequently disassembled

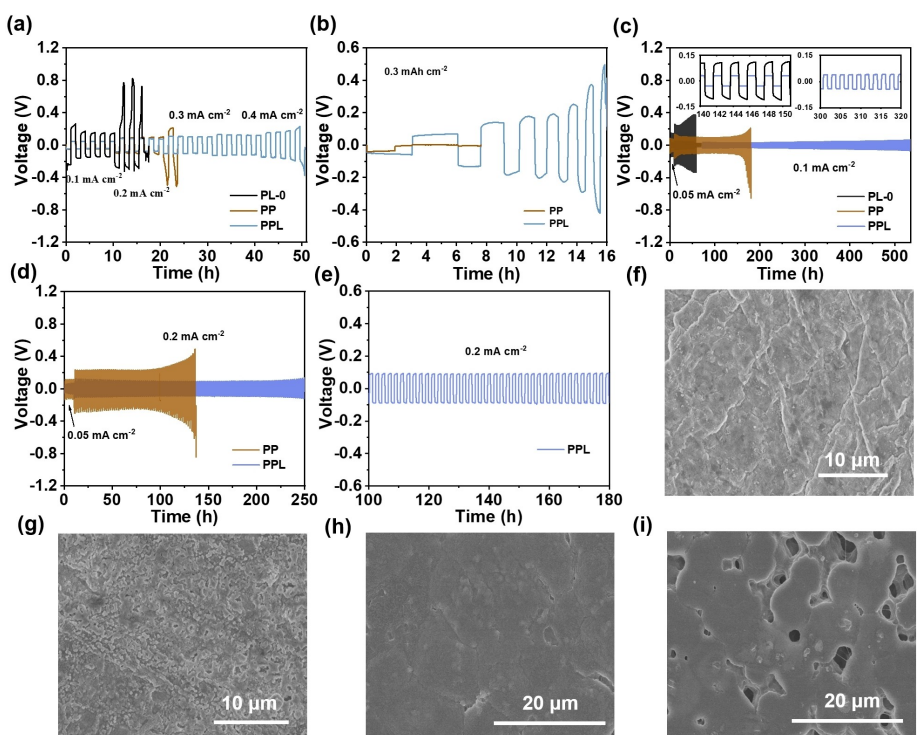


Figure 4. (a) Determination of CCD (time-constant mode) and (c) the lithium stripping-plating profiles at 0.1 mA cm^{-2} of Li|PPL|Li, Li|PP|Li and Li|PL-0|Li cells. (b) Determination of CCD using a capacity-constant mode at 0.3 mAh cm^{-2} with varying current densities from 0.1 to 0.6 mA cm^{-2} of Li|PPL|Li and Li|PP|Li cells. (d, e) The lithium stripping-plating profiles of the Li|PPL|Li and Li|PP|Li cells at 0.2 mA cm^{-2} . Ex situ SEM images of cycled lithium metal recovered from the (f) Li|PPL|Li cell and (g) Li|PP|Li cell. Ex situ SEM images of cycled (h) PPL and (i) PP electrolyte films recovered from the Li|PPL|Li cell and Li|PP|Li cell.

for ex situ SEM characterization of the cycled lithium metal and the bilayer electrolyte films. The digital photographs of recovered PPL, PP membranes and corresponding lithium metals are shown in Figure S5a and b. The surface of cycled lithium metal recovered from the Li|PPL|Li cell is smoother and brighter compared to that of the Li|PP|Li cell. In addition, the cycled PPL film demonstrates much less deformation with respect to that of the cycled PP film, which is attributed to the better mechanical strength of PPL. The SEM images of cycled lithium metal recovered from the Li|PPL|Li cell is presented in Figures 4f and S5c, from which a dense and rather smooth surface is clearly observed favoring for uniform lithium deposition. On the contrary, the cycled lithium metal recovered from the Li|PP|Li cell (Figures 4g and S5d) shows more voids and agglomerated lithium clumps, suggesting non-uniform lithium deposition and striping behavior and stronger interfacial side reactions. Similarly, a much denser and more intact morphology is observed in the cycled PPL membrane (Figures 4h and S5e) compared to the cycled PP membrane (Figures 4i and S5f).

To evaluate the practical applicability of the electrolytes in LMBs, Li|PP|LFP, Li|PPL|LFP and Li|PL-0|LFP full cells were assembled. PPC, as a new type of polycarbonate, has an ester-based polar group in its primary structure, which is capable of trapping and storing liquid electrolytes. As a result, the movement of Li^+ in the polymer can be facilitated by adding a small amount of electrolyte.^[44] Therefore, when assembling the cells, 10 μL of commercial electrolyte was added to the cathode/SSE and anode/SSE interfaces to facilitate the movement of Li^+ within the polymer matrix.

The cyclic voltammetry (CV) curves for the initial three cycles of the Li|PPL|LFP full cell are presented in Figure 5a. The two characteristic peaks observed at 3.28 V and 3.59 V correspond to the reduction potential and oxidation potential of LFP, respectively. No additional peaks can be observed during the cycling process, indicating the absence of side reactions. The CV curves exhibit a high degree of overlap, indicating that the cell exhibits high reversibility that reflects a good electrochemical stability.^[45]

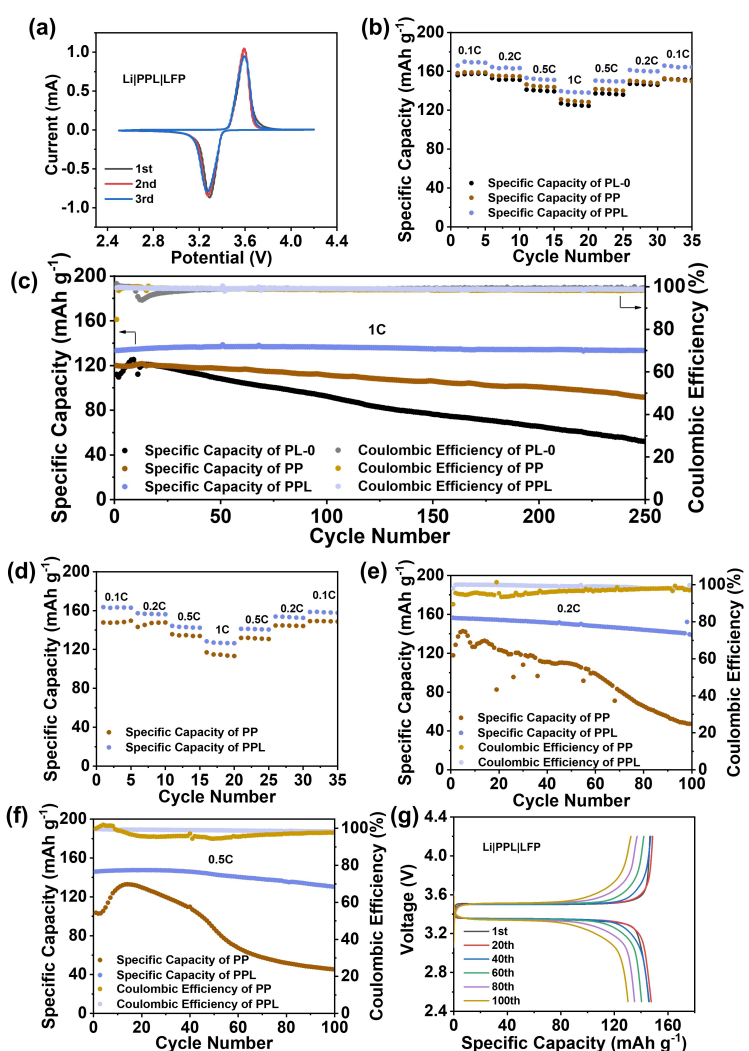


Figure 5. (a) CV curves of the Li|PPL|LFP full cell at a scan rate of 1 mV s^{-1} . (b) Rate capability and (c) cycling performance at 1 C of Li||LFP full cells (filled with 20 μL of electrolyte). (d) Rate capability, (e) cycling performance at 0.2 C, and (f) 0.5 C of Li||LFP full cells (filled with 4 μL of electrolyte). (g) Selected galvanostatic charge-discharge profiles of Li|PPL|LFP full cell at 0.5 C.

The cycling performance of full cells in the voltage range of 2.5–4.2 V was further investigated by galvanostatic charge/discharge tests. Figure 5b illustrates the rate performance of Li|PPL|LFP, Li|PP|LFP, and Li|PL-0|LFP full cells at different current densities (0.1 C, 0.2 C, 0.5 C and 1 C) following a procedure of five charge and discharge cycles. The initial discharge capacities of the Li|PPL|LFP full cell are 165.98, 164.45, 153.22 and 139.66 mAh g⁻¹ at 0.1 C, 0.2 C, 0.5 C and 1 C, respectively. These values are higher than those of the Li|PP|LFP cells (158.06, 155.62, 146.50 and 131.20 mAh g⁻¹), and the Li|PL-0|LFP cells (157.13, 154.33, 147.59, and 139.03 mAh g⁻¹). Figure 5c shows cycling performance at 1 C. The Li|PPL|LFP cell exhibits an initial discharge capacity of 133.38 mAh g⁻¹ and remains relatively stable throughout 250 cycles, retaining a capacity of 133.51 mAh g⁻¹ with a capacity retention ratio of 100.1%. In comparison, the Li|PP|LFP cell demonstrates a lower capacity retention rate of 91.58% (discharge capacity of 120.02 mAh g⁻¹), while the Li|PL-0|LFP cell exhibits a significantly lower capacity retention rate of 46.3% (discharge capacity of 51.90 mAh g⁻¹). In Figure S6, the Li|PL-15|LFP cell not only delivers less initial capacity but also shows stronger capacity decay during prolonged cycling, compared to those of the Li|PPL|LFP cell. This further validates the effectiveness of adopting double layer electrolyte configuration. Therefore, the Li|PPL|LFP cell exhibits not only higher specific discharge capacity but also superior stable cycling performance compared to the Li|PP|LFP and Li|PL-0|LFP cells.

The above experiments show that the bilayer CSEs exhibit better performance. To further explore the potential of the bilayer CSEs for SSLMBs, the content of the added electrolyte was reduced to only 2 µL to each of the cathode/SSE and anode/SSE interfaces. Figure 5d compares the rate performance of Li|PPL|LFP and Li|PP|LFP full cells at different current densities (0.1 C, 0.2 C, 0.5 C, and 1 C). The Li|PPL|LFP cell delivers discharge capacities of 163.54, 157.23, 144.21, and 128.39 mAh g⁻¹, at 0.1 C, 0.2 C, 0.5 C, and 1 C, respectively. In stark contrast, much lower discharge specific capacities are obtained by Li|PP|LFP cell, i.e., 147.74, 143.19, 135.72, and 116.99 mAh g⁻¹. Figure 5e presents a comparison of the cycling performance of the Li|PPL|LFP and Li|PP|LFP full cells at 0.2 C. The former exhibits an initial discharge capacity of 156.49 mAh g⁻¹, with a capacity retention rate of 88.65% over 100 cycles. Compared to the Li|PP|LFP cell (117.82 mAh g⁻¹; 40.17%), the Li|PPL|LFP cell has improved cycling stability and capacity retention due to the positive impact provided by the interconnected LALZNO fillers. Even at 0.5 C (Figure 5f), the Li|PPL|LFP full cell still exhibits an initial specific discharge capacity of 145.92 mAh g⁻¹, and maintains 89.3% of its initial capacity after 100 cycles. The Li|PP|LFP full cell, on the other hand, delivers significantly lower initial specific discharge capacity of 103.67 mAh g⁻¹. Even worse, the capacity starts to decrease sharply after approximately 10 cycles, leading to a retention rate of 43.6% after 100 cycles. Figure 5g shows the charge and discharge profiles of Li|PPL|LFP full cell for the first and every subsequent 20 cycles out of 100 cycles. Notably, the polarization potential is kept at a low value, ca., 0.2 V. The improved cell performance is primarily due to the unique

advantages of LALZNO fiber fillers and the favorable design of the bilayer structure.

Conclusions

In this study, Nb/Al-doped LLZO nanofillers were prepared via electrostatic spinning to construct a bilayer CSE membrane based on PVDF-HFP. The incorporation of LALZNO fillers effectively enhances both the ionic conductivity and Li⁺ transference number of the PVDF-HFP electrolyte. Additionally, it improves the thermal stability and expands the electrochemical stability window of the electrolyte. The bilayer PPL membrane, characterized by its robust mechanical properties, effectively inhibits the growth of lithium dendrites and enhances the stability of lithium cycling. Additionally, the presence of PPC reduces the interface impedance between the CSE and lithium metal, further enhancing the stability. Consequently, the Li|PPL|Li symmetric cell demonstrates stable and uninterrupted cycling for over 520 h during plating and stripping processes, marking a significant advancement over single-layer electrolytes. The bilayer structure, coupled with the incorporation of LALZNO fillers, contributes to enhanced cycle stability in full cells. Specifically, the Li|PPL|LFP cell exhibits an initial discharge specific capacity of 145.92 mAh g⁻¹ at 0.5 C, with 89.3% of capacity retention after 100 cycles. This study highlights the synergistic benefits of combining polymers with inorganic fillers and designing bilayer electrolytes, offering valuable insights into optimizing structures and selecting materials for advanced CSEs.

Experimental Section

Chemicals

Lithium nitrite (LiNO₃), lanthanum nitrite hexahydrate (La(NO₃)₃·6H₂O), aluminum nitrate nonahydrate (Al(NO₃)₃·9H₂O), zirconium propoxide (Zr(C₃H₇O)₄), niobium chloride (NbCl₅), PVDF-HFP (average Mw: ~455,000), poly(vinylpyrrolidone) (PVP) (Mw = 1,300,000), PPC (Mw = 50,000), acetate, and N,N-dimethylformamide (DMF) were supplied from Aladdin. SN (99%) was purchased from Sigma-Aldrich. Lithium bis(trifluoromethanesulfonyl)imide (LiTFSI, 99.99%) was purchased from Guangdong Canrd New Energy Technology Co., Ltd. All the chemicals mentioned above were used directly without any further purification.

Synthesis of LALZNO Nanofibers

LiNO₃, La(NO₃)₃·6H₂O, Zr(C₃H₇O)₄, NbCl₅, and Al(NO₃)₃·9H₂O were dissolved in a mixed solution of DMF and acetic acid, with a molar ratio of Li:La:Zr:Nb:Al of 6.25:3:1.75:0.25:0.25, forming Solution I. Separately, PVP was dissolved in acetic acid and stirred thoroughly at 60 °C for 6 h to obtain the mixed Solution II. The two solutions were mixed in equal volumes and stirred thoroughly to obtain a homogeneous spinning solution, with PVP constituting 10 wt% of the mixture. The spinning solution was loaded into a syringe and then subjected to an electrospinning procedure (Voltage: 19 kV; feeding rate 0.8 mL h⁻¹; distance between the syringe needle and the collector: 15 cm; the speed of the collector: 500 rpm min⁻¹;

temperature: 25 °C and humidity: 30%). A multi-step annealing process was employed for calcination in the air to remove PVP and obtain crystalline LALZNO. Specifically, the sample was heated to and maintained at 300 °C for 2 h to remove PVP, following by increasing the temperature to 750 °C at a heating rate of 2 °C min⁻¹ and holding for 2 h to crystallize the LALZNO.

Synthesis of Monolayer CSE

Monolayer CSE membranes were prepared by a solution casting method. Firstly, PVDF-HFP and LiTFSI were dissolved in DMF and then subjected to sonication. Subsequently, different proportions of LALZNO nanofibers (0 wt%, 5 wt%, 10 wt%, 15 wt%, 20 wt%) were added to the above solution, which was magnetically stirred to form a homogeneous mixture. Finally, the solution was cast onto a pre-cleaned polytetrafluoroethylene (PTFE) plastic mold with a fixed thickness of 500 μm, and then dried in a vacuum oven at 80 °C for 12 h. The dried membranes, were peeled off from the PTFE, and labeled as PL-0, PL-5, PL-10, PL-15, and PL-20, corresponding to the respective filler contents.

Synthesis of Bilayer CSE

Bilayer CSE membranes were prepared also by a solution casting method, involving two distinct solutions (Solution A and B). Solution A was prepared by firstly dissolving PVDF-HFP/PPC (weight ratio 1:1) and 50 wt% of LiTFSI (relative to PVDF-HFP/PPC mass ratio) in DMF while stirring at 50 °C for 3 h. Then, 10 wt% of LALZNO filler was dispersed into the above solution under magnetic stirring for 12 h. Solution B was prepared by firstly dissolving PVDF-HFP/LiTFSI (1:1) and SN (20 wt% relative to PVDF-HFP) in DMF under stirring at 50 °C for 3 h, then incorporating 15 wt% of LALZNO filler into the above solution under magnetic stirring for 12 h. Solution A was first cast onto a pre-cleaned PTFE sheet with a thickness of 250 μm. The wet membrane was then dried in a vacuum oven at 80 °C for 1 h. Afterwards, solution B was cast onto the surface of the dried membrane to achieve a wet thickness of 500 μm. The wet membrane was then dried in a vacuum oven at 60 °C for 12 h to obtain the bilayer CSE membrane. The final dried membrane (denoted as PPL) was peeled off from the PTFE sheet and further dried in a vacuum oven at 60 °C for 12 h to remove residual DMF. For comparison, a bilayer pure polymer membrane without LALZNO nanofibers (denoted as PP) prepared by same procedures as described earlier was subjected control tests under identical conditions.

Material Characterizations

Surface morphologies and elemental distributions of the CSE membranes and LALZNO nanofibers were analyzed using a scanning electron microscope (SEM, SU8020, Hitachi) coupled with an EDS. The crystal structure of all samples were determined by X-ray diffractometer (XRD; X'Pert PRO) with a Cu Kα radiation source ($\lambda = 1.5406 \text{ \AA}$). Micro-Raman spectroscopy (WITec alpha 300 R) was performed to characterize the LALZNO powder. FT-IR analysis of the CSE membranes was recorded with a PerkinElmer spectrometer (L1600400 spectrum Two DTGS). Thermogravimetric analysis (TG, TGA-Q500 instrument) was conducted in a N₂ atmosphere with a heating rate of 10 °C min⁻¹ from 90 to 700 °C. Stress-strain test was conducted using an electronic universal testing machine (AGS-J10). X-ray photoelectron spectroscopy (XPS, ESCALAB 250Xi) was used to examine the elemental compositions at the surfaces of LALZNO fillers.

Electrochemical Performance Tests

Electrochemical impedance spectroscopy (EIS, Solartron 3000 A) was performed to evaluate the ionic conductivities of CSEs by assembling SS|CSE|SS symmetric blocking cells with a frequency range of 7 MHz ~1 Hz and a potential amplitude of 10 mV. Ionic conductivity was calculated using Equation (1):

$$\sigma = \frac{L}{A R} \quad (1)$$

Where σ (S cm⁻¹), L (cm), A (cm²), and R (Ω) represent the ionic conductivity, the membrane thickness, the contact area between the membrane and stainless-steel, and bulk resistance, respectively.

Further, the ionic conductivities at various temperatures were tested and the ion mobilization activation energy was calculated according to the Arrhenius Equation (2):

$$\sigma T = A \exp\left(-\frac{E_a}{kT}\right) \quad (2)$$

Where A is the pre-exponential constant, E_a (eV) is the energy of activation, k (J K⁻¹) is the Boltzmann constant, and T (K) is the thermodynamic temperature.

The Li⁺ transference number (t_{Li^+}) was calculated based on the Evans-Vincent-Bruce method in a symmetric Li|CSE|Li cell configuration, according to Equation (3):

$$t_{Li^+} = \frac{I_s(\Delta V - I_0 R_0)}{I_0(\Delta V - I_s R_s)} \quad (3)$$

Where ΔV (mV) is the voltage polarization applied, I_s (μA) and R_s (Ω) are the steady-state current and impedance, and I_0 and R_0 are the initial current and resistance, respectively.

LSV was performed in SS|CSE|Li cells in the potential range from 3.0 to 5.2 V with a scan rate of 0.1 mV s⁻¹ at room temperature. The CV test was carried out in Li|CSE|LFP full cells (voltage: 2.5–4.2 V; scan rate: 0.05 mV s⁻¹). All rate and cycling performance of full cells were tested by constant current discharge/charge experiments with a battery test system (Neware CT-4000 Battery Test System) at 25 °C.

Acknowledgements

This work is supported by the National Natural Science Foundation of China (52277215 and 52377206), the Postdoctoral Science Foundation of China (2023 M730884), and the Postdoctoral Science Foundation of Heilongjiang Province of China (LBH. Z23024).

Conflict of Interests

The authors declare no conflict of interest.

Data Availability Statement

The data that support the findings of this study are available from the corresponding author upon reasonable request.

Keywords: Lithium metal batteries • Bilayer composite solid electrolyte • PVDF-HFP • LALZNO nanofiber fillers • Electrostatic spinning technology

- [1] S. Chu, A. Majumdar, *Nature* **2012**, 488(7411), 294–303.
- [2] J. J. Xu, X. Y. Cai, S. M. Cai, Y. X. Shao, C. Hu, S. R. Lu, S. J. Ding, *Energy Environ. Mater.* **2023**, 6(5), e12450.
- [3] A. Masias, J. Marcicki, W. A. Paxton, *ACS Energy Lett.* **2021**, 6(2), 621–630.
- [4] S. Kim, G. Park, S. J. Lee, S. Seo, K. Ryu, C. H. Kim, J. W. Choi, *Adv. Mater.* **2023**, 35(43), 2206625.
- [5] M. Walter, M. V. Kovalenko, K. V. Kravchyk, *New J. Chem.* **2020**, 44(5), 1677–1683.
- [6] Z. A. Ghazi, Z. H. Sun, C. G. Sun, F. L. Qi, B. G. An, F. Li, H. M. Cheng, *Small* **2019**, 15(32), 1900687.
- [7] Y. P. Guo, H. Q. Li, T. Y. Zhai, *Adv. Mater.* **2017**, 29(29), 1700007.
- [8] H. C. Wang, L. Sheng, G. Yasin, L. Wang, H. Xu, X. M. He, *Energy Storage Mater.* **2020**, 33, 188–215.
- [9] J. W. Zhang, Y. Li, Z. Chen, Q. Liu, Q. G. Chen, M. H. Chen, *Energy Environ. Mater.* **2023**, 6(6), e12573.
- [10] L. S. Li, Y. F. Deng, G. H. Chen, *J. Energy Chem.* **2020**, 50, 154–177.
- [11] X. Wang, Z. Chen, S. S. Qiu, Q. Liu, X. Q. Liang, J. Y. Cui, M. H. Chen, *ACS Appl. Energ. Mater.* **2023**, 7(2), 689–696.
- [12] Y. X. Wu, Y. Li, Y. Wang, Q. Liu, Q. G. Chen, M. H. Chen, *J. Energy Chem.* **2022**, 64, 62–84.
- [13] X. Wang, Z. Chen, K. Jiang, M. H. Chen, S. Passerini, *Adv. Energy Mater.* **2024**, 14(19), 2304229.
- [14] Y. L. Liu, H. Y. Xu, W. N. Liu, G. H. Li, X. Liu, M. H. Chen, Z. Chen, *Energy Fuels* **2023**, 37(23), 18154–18162.
- [15] Y. X. Wu, Z. Chen, Y. Wang, Y. Li, C. X. Zhang, Y. H. Zhu, Z. Y. Yue, X. Liu, M. H. Chen, *J. Energy Chem.* **2024**, 89, 437–448.
- [16] Y. Li, J. Y. Cai, J. W. Zhang, Z. Chen, G. M. Wang, Q. G. Chen, M. H. Chen, *Adv. Energy Mater.* **2023**, 13(14), 2204114.
- [17] M. H. Chen, W. N. Liu, Z. Y. Yue, Y. Wang, Y. X. Wu, Y. Li, Z. Chen, *Batteries* **2023**, 9(5), 270.
- [18] Y. Wang, Z. Chen, Y. X. Wu, Y. Li, Z. Y. Yue, M. H. Chen, *ACS Appl. Mater. Interfaces* **2023**, 15(17), 21526–21536.
- [19] S. M. Su, J. B. Ma, L. Zhao, K. Lin, Q. D. Li, S. S. Lv, F. Y. Kang, Y. B. He, *Carbon Energy* **2021**, 3(6), 866–894.
- [20] K. G. Kumar, P. B. Bhargav, C. Balaji, A. Nafis, K. Aravindh, P. Ramasamy, *J. Electrochem. Energy Convers. Storage* **2021**, 18(3), 031012.
- [21] D. X. Cao, X. Sun, Q. Li, A. Natan, P. Y. Xiang, H. L. Zhu, *Matter* **2020**, 3(1), 57–94.
- [22] Y. Wang, Z. Chen, K. Jiang, Z. Shen, S. Passerini, M. Chen, *Small* **2024**, 20(35), e2402035.
- [23] Q. Liu, Z. Geng, C. P. Han, Y. Z. Fu, S. Li, Y. B. He, F. Y. Kang, B. H. Li, *J. Power Sources* **2018**, 389, 120–134.
- [24] Y. F. Wang, T. Liu, C. W. Liu, G. Q. Liu, J. K. Yu, Q. J. Zou, *Solid State Ionics* **2022**, 378, 115897.
- [25] C. Y. Yan, P. Zhu, H. Jia, Z. Du, J. D. Zhu, R. Orenstein, H. Cheng, N. Q. Wu, M. Dirican, X. W. Zhang, *Energy Storage Mater.* **2020**, 26, 448–456.
- [26] M. H. Chen, Z. Y. Yue, Y. X. Wu, Y. Wang, Y. Li, Z. Chen, *Sustainable Mater. Technol.* **2023**, 36, e00587.
- [27] Y. N. Teng, H. Liu, Q. Wang, Y. He, Y. C. Hua, C. P. Li, J. Bai, *J. Energy Storage* **2024**, 76, 109784.
- [28] H. L. Nguyen, V. T. Luu, M. C. Nguyen, S. H. Kim, Q. H. Nguyen, N. I. Nungu, Y. S. Jun, W. Ahn, *Adv. Funct. Mater.* **2022**, 32(45), 2207874.
- [29] Y. Li, W. Zhang, Q. Q. Dou, K. W. Wong, K. M. Ng, *J. Mater. Chem. A* **2019**, 7(7), 3391–3398.
- [30] T. H. Mengesha, S. L. Beshahwured, S. H. Wu, Y. S. Wu, R. Jose, S. J. Lue, C. C. Yang, *ACS Appl. Energ. Mater.* **2021**, 4(12), 14554–14574.
- [31] K. G. Kumar, P. B. Bhargav, C. Balaji, A. Nafis, K. Aravindh, P. Ramasamy, *J. Electrochem. Energy Convers. Storage* **2021**, 18(3), 031012.
- [32] J. G. Connell, Y. S. Zhu, P. Zapol, S. Tepavicevic, A. Sharifi, J. Sakamoto, L. A. Curtiss, D. D. Fong, J. W. Freeland, N. M. Markovic, *ACS Appl. Mater. Interfaces* **2018**, 10(20), 17471–17479.
- [33] Y. Horowitz, M. Lifshitz, A. Greenbaum, Y. Feldman, S. Greenbaum, A. P. Sokolov, D. Golodnitsky, *J. Electrochem. Soc.* **2020**, 167(16), 160514.
- [34] Z. Q. Fang, M. Zhao, Y. Peng, S. Y. Guan, *ACS Appl. Mater. Interfaces* **2022**, 14(16), 18922–18934.
- [35] X. W. Yu, A. Manthiram, *Energy Storage Mater.* **2021**, 34, 282–300.
- [36] Z. Chen, G. T. Kim, J. K. Kim, M. Zarrabeitia, M. Kuenzel, H. P. Liang, D. Geiger, U. Kaiser, S. Passerini, *Adv. Energy Mater.* **2021**, 11(30), 2101339.
- [37] C. Wang, H. R. Zhang, J. D. Li, J. C. Chai, S. M. Dong, G. L. Cui, *J. Power Sources* **2018**, 397, 157–161.
- [38] Z. Chen, G. T. Kim, D. Bresser, T. Diemant, J. Asenbauer, S. Jeong, M. Copley, R. J. Behm, J. Lin, Z. X. Shen, S. Passerini, *Adv. Energy Mater.* **2018**, 8(27), 1801573.
- [39] K. L. Luo, L. G. Yi, X. Y. Chen, L. Yang, C. F. Zou, X. Y. Tao, H. Li, T. J. Wu, X. Y. Wang, *J. Electroanal. Chem.* **2021**, 895, 115462.
- [40] F. Chen, J. Luo, M. X. Jing, J. Li, Z. H. Huang, H. Yang, X. Q. Shen, *J. Electrochem. Soc.* **2021**, 168(7), 070513.
- [41] X. Y. Huang, S. S. Zeng, J. J. Liu, T. He, L. Y. Sun, D. H. Xu, X. Y. Yu, Y. Luo, W. Y. Zhou, J. F. Wu, *J. Phys. Chem. C* **2015**, 119(50), 27882–27891.
- [42] F. Chen, M. X. Jing, H. Yang, W. Y. Yuan, M. Q. Liu, Y. S. Ji, S. Hussain, X. Q. Shen, *Ionics* **2021**, 27(3), 1101–1111.
- [43] M. Arrese-Igor, M. Martinez-Ibañez, E. Pavlenko, M. Forsyth, H. J. Zhu, M. Armand, F. Agusse, P. López-Aranguren, *ACS Energy Lett.* **2022**, 7(4), 1473–1480.
- [44] L. D. Y. Wang, D. Liu, T. Huang, Z. Geng, A. S. Yu, *RSC Adv.* **2020**, 10(17), 10038–10045.
- [45] S. Wang, Q. F. Sun, Q. Zhang, C. Li, C. R. Xu, Y. Ma, X. X. Shi, H. Z. Zhang, D. W. Song, L. Q. Zhang, *Adv. Energy Mater.* **2023**, 13(16), 2204036.

Manuscript received: June 12, 2024

Revised manuscript received: August 6, 2024

Accepted manuscript online: August 14, 2024

Version of record online: October 17, 2024